

A hydromechanical approach for anisotropic elasto-viscoplastic geomaterials: Application to underground excavations in sedimentary rocks

Mohamed Mahjoub, Ahmed Rouabhi

▶ **To cite this version:**

Mohamed Mahjoub, Ahmed Rouabhi. A hydromechanical approach for anisotropic elasto-viscoplastic geomaterials: Application to underground excavations in sedimentary rocks. Underground Space, 2018, 10.1016/j.undsp.2018.06.001 . hal-01884690

HAL Id: hal-01884690

https://minesparis-psl.hal.science/hal-01884690

Submitted on 22 Oct 2021

HAL is a multi-disciplinary open access archive for the deposit and dissemination of scientific research documents, whether they are published or not. The documents may come from teaching and research institutions in France or abroad, or from public or private research centers.

L'archive ouverte pluridisciplinaire **HAL**, est destinée au dépôt et à la diffusion de documents scientifiques de niveau recherche, publiés ou non, émanant des établissements d'enseignement et de recherche français ou étrangers, des laboratoires publics ou privés.



Distributed under a Creative Commons Attribution - NonCommercial 4.0 International License

Version of Record: https://www.sciencedirect.com/science/article/pii/S2467967418300266
Manuscript_93be885b6e9b8ee17f04f73fe15a84b0

A hydromechanical approach for anisotropic elasto-viscoplastic geomaterials: application to underground excavations in sedimentary rocks

Abstract

To better describe excavation operations in deep geological formations, several aspects should be considered, especially the material anisotropy, time-dependent behavior, and hydromechanical coupling. In the present paper, a hydromechanical model based on the framework of continuous porous media was proposed. The mechanical elasto-viscoplastic constitutive model accounted for the material elastic and non-elastic anisotropies, using a transformation between the real transversely isotropic material and a fictitious isotropic material. Considering the hydraulic behavior, the permeability was expressed as a function of the volumetric viscoplastic strain. The model was applied to a case study of two tunnel excavations in an anisotropic rock under an initial anisotropic stress state. The results of the numerical simulations using a finite element code were in good agreement with the field convergence and permeability data.

Keywords:

Hydromechanical behavior, Transverse isotropy, Tunnel excavation, Viscoplasticity, Permeability

© 2018 published by Elsevier. This manuscript is made available under the CC BY NC user license
https://creativecommons.org/licenses/by-nc/4.0/

1. Introduction

During tunnel constructions and drift excavations, the analysis of *in situ* measurements, such as convergence and permeability, represents a key step for the choice of the appropriate support and reinforcement installations (Gesta, 1994; Panet, 1995). This information is even more important when the rock formation exhibits time-dependent behavior, which may be due to both the viscoplastic behavior of the surrounding rock formation and the hydromechanical coupling with the ground water (Barla, 2001; Prassetyo and Gutierrez, 2016; Rahal et al., 2017; Soga et al., 2017).

Construction operations become even more challenging when the rock is squeezing in a non-symmetric manner, *i.e.*, the convergence measurements are anisotropic (Armand et al., 2013; Guayacán-Carrillo et al., 2016; Manh et al., 2014; Panet, 1996; Vu et al., 2013b; Wang and Huang, 2011). In those situations, dedicated numerical tools and constitutive models are needed the most to better understand the involved mechanisms, and thus, provide accurate predictions to assist the excavation monitoring.

The dissymmetric convergence observations could be explained by the formation heterogeneities and discontinuities and the different problem anisotropies, namely, the initial stress state and material elastic and non-elastic anisotropies. These factors are more or less important depending on the studied case. The effect of the elastic anisotropy on tunnel behavior has been studied by several authors such as Bertrand and Collin (2017), Kim et al. (2005), Klopčič and Logar (2014), Plana et al. (2004), Tao and Bobet (2016), Tonon and Amadei (2002, 2003), and Vu et al. (2013a). The non-elastic anisotropy was used by Martín et al. (2011) and Manh et al. (2015) to reproduce the dissymmetric

convergence measurements in different front positions of a tunnel. The presence of discontinuities (rock joints) was studied by Zhuang et al. (2014) to reproduce the thermodynamic behavior of gas storage caverns.

Recently, a multitude of studies (Barla et al., 2010; Bonini et al., 2009; Pellet, 2009; Cuvilliez et al., 2017; Souley et al., 2017) employed elasto-visco-plastic isotropic models to describe the long-term behavior of the rock formation around tunnels. However, these models are not accurate enough to reproduce the squeezing dissymmetry owing to the material anisotropy. Some other recent studies were interested in the effect of the material anisotropy on tunnels behavior. Tao and Bobet (2016) and Tonon and Amadei (2002, 2003) , for example, studied the effect of the bedding orientation on the stress and displacement around the tunnels, but they considered only linear elastic materials. Bertrand and Collin (2017) used an elasto-plastic model to study the shear banding around tunnels; and Klopčič and Logar (2014) and Plana et al. (2004) used the same type of modeling to study the displacements. These models are, however, adapted only for the analysis of the short-term response of the material. Other authors such as Manh et al. (2015), Mánica et al. (2016, 2017), Pardoen et al. (2016), and Pardoen and Collin (2017) developed elasto-visco-plastic models for transversely isotropic materials. However, in those models the non-elastic anisotropy, considered only through yield functions, involves generally a certain number of parameters with no clear physical meaning, which are difficult to identify by conventional triaxial tests.

In this study, a new hydromechanical model accounting for elastic and non-elastic anisotropies, time-dependency, and permeability alteration was

proposed. The model, built within the theoretical framework of continuous porous media, was based on an approach that reduces the number of anisotropy parameters and simplifies their identification, yet its predictive capacities were ensured. For the mechanical behavior, an equivalent material approach was used to derive a viscoplastic model for transversely isotropic materials; and for the hydraulic behavior, the permeability was expressed as a function of the volumetric viscoplastic strain to account for the alteration of the hydraulic transfer properties around the tunnels. To validate the developed model, a case study of two tunnels excavated in an anisotropic rock under an anisotropic initial stress state was considered. The studied tunnels are in two perpendicular directions, following the minor and major initial horizontal stresses.

This paper is organized as follows. First, the hydromechanical model is described; the equivalence approach between isotropy and transverse isotropy is explained and the viscoplastic strain, permeability, and porosity evolution laws are presented. Then, the case study is discussed and the obtained numerical results are compared to the available experimental data.

Notations. Throughout this paper, first-order tensors (vectors) are represented by an arrow over a letter ($\vec{a}$), second-order tensors are denoted by two lines under a letter ($\underline{\underline{a}}$), and fourth-order tensors are designated by a tilde beneath a letter ($\underset{\sim}{A}$). The second-order identity tensor is denoted by $\underline{\underline{1}}$. The symbol ':' denotes the product with double contraction, e.g., $\underline{\underline{a}} : \underline{\underline{b}} = a_{ij} b_{ji}$, where the index denotes the Cartesian components, and repeated subscripts imply summation. The product $\underline{\underline{a}}\,\underline{\underline{b}}$ denotes a single contraction, *i.e.*, $(\underline{\underline{a}}\,\underline{\underline{b}})_{ij} = a_{ik} b_{kj}$. In the same manner, the product $\underset{\sim}{A}\underset{\sim}{B}$ is defined

as $(\underset{\sim}{A}\underset{\sim}{B})_{\mathrm{ijkl}} = A_{\mathrm{ijmn}}B_{\mathrm{nmkl}}$. For a tensor $\underline{\underline{a}}$, $\mathrm{tr}(\underline{\underline{a}})$ is its trace, $\|\underline{\underline{a}}\| = \sqrt{\underline{\underline{a}} : \underline{\underline{a}}}$ is its norm, and $\underline{\underline{a}}' = \underline{\underline{a}} - (\mathrm{tr}(\underline{\underline{a}})/3)\underline{\underline{1}}$ is its deviatoric part.

2. A hydromechanical model accounting for material anisotropy and permeability alteration

The hydromechanical model introduced in this paper is based on the theoretical framework of continuous porous media. Stress partition between the solid matrix and fluid phases was applied in such a way that the mechanical behavior of the solid matrix could be defined regardless of the flowing fluids in the porous space. To define that mechanical behavior for transversely isotropic materials, an equivalent material approach was used and a viscoplastic model was built. The impact of the mechanical behavior on the hydraulic properties was considered by allowing the intrinsic permeability alteration.

2.1. Macroscopic balance equations

To describe the problem of tunnel excavations, the rock was considered as a saturated porous medium composed of a solid matrix σ and a liquid phase λ. For a quantity $\varphi(\vec{x}, t)$ attached to the porous medium, function of the position vector $\vec{x}$ and time t, its material derivative is given by $\dot{\varphi} = \dfrac{\partial \varphi}{\partial t} + \vec{v} \cdot \vec{\nabla}\varphi$, where $\vec{v}$ is the solid matrix velocity. When referring to the solid matrix movement, the mass and momentum balance equations could be written in the following form:

$$\begin{aligned} \dot{m}^{\lambda}/J + \vec{\nabla} \cdot \left(\rho_{\lambda} \vec{w}^{\lambda}\right) &= 0 \\ \vec{\nabla} \cdot \underline{\underline{\sigma}} + \rho \vec{g} &= \vec{0} \end{aligned} \tag{1}$$

$$\text{with} \quad m^{\lambda} = Jn\rho_{\lambda} \quad \text{and} \quad \rho = n\rho_{\lambda} + (1-n)\rho_{\sigma}$$

where J is the Jacobian of the solid transformation, n is the porosity, ρ_{α} is the mass density of the α-phase ($\alpha = \sigma, \lambda$), $\vec{w}^{\lambda}$ is the filtration or Darcy's velocity of the liquid phase, $\underline{\underline{\sigma}}$ is the Cauchy total stress tensor acting on both liquid and solid phases, and $\vec{g}$ is the gravitational field vector.

2.2. Mechanical behavior

The concept of the effective stress acting on the solid matrix (Coussy, 1991) was used as follows :

$$\dot{\underline{\underline{\hat{\sigma}}}} = \dot{\underline{\underline{\sigma}}} + b\dot{p}\underline{\underline{1}} \tag{2}$$

where $\underline{\underline{\sigma}}$ is the total Cauchy stress tensor (the same as in equation (1)), $\underline{\underline{\hat{\sigma}}}$ is the effective stress tensor, p is the pore pressure, and b is the Biot coefficient (Biot, 1941).

Given the complexity to define new mechanical constitutive models for anisotropic materials, an equivalence approach was employed in this work allowing us to take advantage of the well-established isotropic theory. This modeling procedure consists in defining a fictitious isotropic material and transferring its behavior law, by means of a tensorial transformation, to the real transversely isotropic material. This method was first introduced in a previous work (Mahjoub et al., 2015) and was used to interpret only laboratory experiments. Compared to that work, the equivalence approach was extended in the present study to elasto-viscoplastic models and was employed to simulate real scale excavation problems. The main features of this modeling procedure are presented in the next subsection with the aim

to use it to define a new behavior law for anisotropic materials. In this work, we restrict ourselves to the case of transverse isotropy, knowing that the presented methodology can be applied for any anisotropy.

2.2.1. Isotropy-transverse isotropy transformation

Consider a real elastic transversely isotropic material whose effective stress, elastic strain, and Hooke's tensors are denoted by $\underline{\underline{\hat{\sigma}}}$, $\underline{\underline{\varepsilon}}_{\mathrm{e}}$, and $\underset{\sim}{H}(E, E', \nu, \nu', G)$, respectively, and a fictitious elastic isotropic material whose corresponding tensors are denoted by $\underline{\underline{\bar{\sigma}}}$, $\underline{\underline{\bar{\varepsilon}}}_{\mathrm{e}}$, and $\underset{\sim}{\bar{H}}(\bar{E}, \bar{\nu})$, respectively. The definition of the real elastic parameters E, E', ν, ν', and G is clarified by providing the matrix form of the compliance tensor $\underset{\sim}{H}^{-1}$ as follows:

$$H^{-1} = \begin{pmatrix} \frac{1}{E} & -\frac{\nu}{E} & -\frac{\nu'}{E'} & 0 & 0 & 0 \\ -\frac{\nu}{E} & \frac{1}{E} & -\frac{\nu'}{E'} & 0 & 0 & 0 \\ -\frac{\nu'}{E'} & -\frac{\nu'}{E'} & \frac{1}{E'} & 0 & 0 & 0 \\ 0 & 0 & 0 & \frac{1+\nu}{E} & 0 & 0 \\ 0 & 0 & 0 & 0 & \frac{1}{2G} & 0 \\ 0 & 0 & 0 & 0 & 0 & \frac{1}{2G} \end{pmatrix} \tag{3}$$

in which the normal vector to the bedding plane $\vec{e}$ coincides with the vector $\vec{e}_3$ of the orthonormal basis $(\vec{e}_1, \vec{e}_2, \vec{e}_3)$ of $\mathbb{R}^3$. Obviously, the compliance tensor of an isotropic material can be deduced by setting $E = E'$, $\nu = \nu'$, and $2G = E/(1+\nu)$.

The real and fictitious stress tensors can be related by a second-order tensorial transformation function $\underline{\underline{\ell}}$ such that $\underline{\underline{\bar{\sigma}}} = \underline{\underline{\ell}}(\underline{\underline{\hat{\sigma}}})$. Depending on the choice of $\underline{\underline{\ell}}$, one may introduce different models to transform the real anisotropic to a

fictitious isotropic material. Here, $\underline{\underline{\ell}}$ is assumed linear to simplify the parameter identification and numerical implementation in computer codes. With the linearity assumption, $\underline{\underline{\ell}}$ may be represented using a symmetric positive definite fourth-order tensor $\underline{\underline{L}}$:

$$\underline{\underline{\bar{\sigma}}} = \underline{\underline{L}} : \underline{\underline{\hat{\sigma}}} \tag{4}$$

The equivalence of elastic energy $\underline{\underline{\bar{\sigma}}} : \underline{\underline{\bar{\varepsilon}}}_{\mathrm{e}} = \underline{\underline{\hat{\sigma}}} : \underline{\underline{\varepsilon}}_{\mathrm{e}}$ was employed to relate the real and fictitious strains and to ensure the symmetry of the equivalent stiffness tensor, leading to

$$\underline{\underline{\varepsilon}}_{\mathrm{e}} = \underline{\underline{L}} : \underline{\underline{\bar{\varepsilon}}}_{\mathrm{e}} \tag{5}$$

Combining equations (4) and (5), and given that $\underline{\underline{\bar{\sigma}}} = \underline{\underline{\bar{H}}} : \underline{\underline{\bar{\varepsilon}}}_{\mathrm{e}}$, it follows that

$$\underline{\underline{\bar{H}}} = \underline{\underline{L}}\,\underline{\underline{H}}\,\underline{\underline{L}} \tag{6}$$

This equation could be restated in the form $\underline{\underline{H}}^{-1} = \underline{\underline{L}}\,\underline{\underline{\bar{H}}}^{-1}\underline{\underline{L}}$. When multiplied at left and at right by $\underline{\underline{\bar{H}}}^{-\frac{1}{2}}$, and given that $\underline{\underline{\bar{H}}}^{-1} = \underline{\underline{\bar{H}}}^{-\frac{1}{2}}\underline{\underline{\bar{H}}}^{-\frac{1}{2}}$, it reads $\underline{\underline{\bar{H}}}^{-\frac{1}{2}}\underline{\underline{H}}^{-1}\underline{\underline{\bar{H}}}^{-\frac{1}{2}} = (\underline{\underline{\bar{H}}}^{-\frac{1}{2}}\underline{\underline{L}}\,\underline{\underline{\bar{H}}}^{-\frac{1}{2}})^2$. The expression of $\underline{\underline{L}}$ could then be deduced as a function of $\underline{\underline{H}}$ and $\underline{\underline{\bar{H}}}$, as follows:

$$\underline{\underline{L}} = \underline{\underline{\bar{H}}}^{\frac{1}{2}} \left(\underline{\underline{\bar{H}}}^{-\frac{1}{2}} \underline{\underline{H}}^{-1} \underline{\underline{\bar{H}}}^{-\frac{1}{2}} \right)^{\frac{1}{2}} \underline{\underline{\bar{H}}}^{\frac{1}{2}} \tag{7}$$

Note that equation (6) was restated because it is easier to calculate the square root of an isotropic tensor ($\underline{\underline{\bar{H}}}$ or $\underline{\underline{\bar{H}}}^{-1}$) rather than a transverse

isotropic tensor. It is clear from equation (7) that the $\underset{\sim}{L}$-transformation is a function of the real (E, E', ν, ν', and G) and fictitious ($\bar{E}$, and $\bar{\nu}$) elastic parameters and the bedding plane orientation ($\vec{e}$) only (see Appendix A for the mathematical details).

2.2.2. Elasto-viscoplastic model

In this work, a viscoplastic law was proposed to model the mechanical behavior of the solid matrix. It could be written in the following form:

$$\underset{\approx}{\hat{\sigma}} - \underset{\approx}{\hat{\sigma}}_0 = \underset{\sim}{H} : \left(\underset{\approx}{\varepsilon} - \underset{\approx}{\varepsilon}_{\mathrm{vp}}\right) \tag{8}$$

where $\underset{\sim}{H}$ is the Hooke's tensor introduced earlier, $\underset{\approx}{\hat{\sigma}}_0 = \underset{\approx}{\hat{\sigma}}(t=0)$ is the initial stress tensor, and $\underset{\approx}{\varepsilon}_{\mathrm{vp}}$ is the viscoplastic part of the total strain tensor $\underset{\approx}{\varepsilon}$.

The mechanical model was adapted to transversely isotropic materials using the modeling approach described above. To ensure the equivalence between the real and the fictitious materials, a constant $\underset{\sim}{L}$-transformation is employed. This transformation, which was determined based on elasticity, is therefore used for the elasto-viscoplastic model.

The fictitious effective stress $\underset{\approx}{\bar{\sigma}}$, elastic strain $\underset{\approx}{\bar{\varepsilon}}_{\mathrm{e}}$, viscoplastic strain $\underset{\approx}{\bar{\varepsilon}}_{\mathrm{vp}}$, and Hooke's $\underset{\sim}{\bar{H}}$ tensors can be related to the real quantities $\underset{\approx}{\hat{\sigma}}$, $\underset{\approx}{\varepsilon}_{\mathrm{e}}$, $\underset{\approx}{\varepsilon}_{\mathrm{vp}}$, and $\underset{\sim}{H}$, respectively, using the equivalence relations $\underset{\approx}{\bar{\sigma}} = \underset{\sim}{L} : \underset{\approx}{\hat{\sigma}}$, $\underset{\approx}{\varepsilon}_{\mathrm{e}} = \underset{\sim}{L} : \underset{\approx}{\bar{\varepsilon}}_{\mathrm{e}}$, $\underset{\approx}{\varepsilon}_{\mathrm{vp}} = \underset{\sim}{L} : \underset{\approx}{\bar{\varepsilon}}_{\mathrm{vp}}$, and $\underset{\sim}{\bar{H}} = \underset{\sim}{L}\underset{\sim}{H}\underset{\sim}{L}$ (see Fig. 1). Using this approach, the model accounts for the anisotropy of the non-elastic parameters in addition to the anisotropy of the elastic parameters.

The use of the equivalence approach implies that the behavior law of the

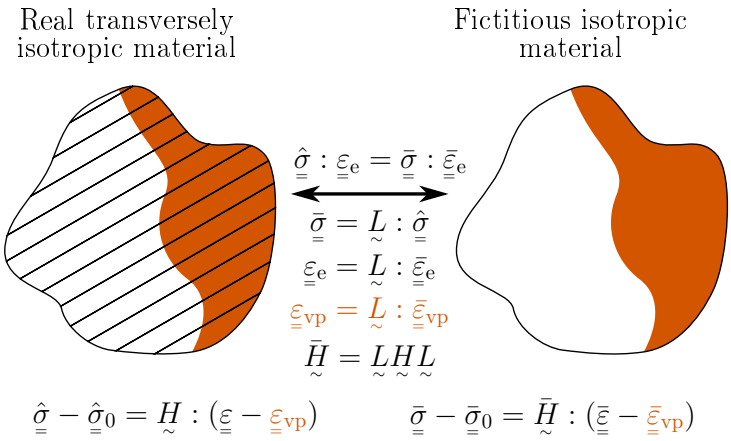


Figure 1: Schematic representation of the real transversely isotropic and fictitious isotropic materials with the equivalence relations.

equivalent isotropic material could be written in the same form,

$$\bar{\underline{\underline{\sigma}}} - \bar{\underline{\underline{\sigma}}}_0 = \bar{\underset{\sim}{H}} : \left(\bar{\underline{\underline{\varepsilon}}} - \bar{\underline{\underline{\varepsilon}}}_{\mathrm{vp}}\right) \tag{9}$$

Hence, one has only to define the behavior law of the fictitious isotropic material and obtain a model for the real transversely isotropic material according to the equivalence relations.

Following the line of thought explained above, the evolution of the viscoplastic strain is ensured by an evolution law of the fictitious viscoplastic strain such that

$$\underline{\underline{\varepsilon}}_{\mathrm{vp}} = \underset{\sim}{L} : \bar{\underline{\underline{\varepsilon}}}_{\mathrm{vp}} \quad \text{with} \quad \dot{\underline{\underline{\varepsilon}}}_{\mathrm{vp}} = \dot{\underline{\underline{\varepsilon}}}_{\mathrm{vp}}(\bar{\underline{\underline{\sigma}}}) \tag{10}$$

In this work, the evolution law of $\bar{\underline{\underline{\varepsilon}}}_{\mathrm{vp}}$ was based on the Perzyna non-

associated model and it can be written as follows:

$$\dot{\underline{\underline{\varepsilon}}}_{\text{vp}} = A \left\langle \frac{\bar{F}(\underline{\underline{\bar{\sigma}}}, \bar{\xi})}{F_0} \right\rangle^m \partial_{\underline{\underline{\bar{\sigma}}}} \bar{G}(\underline{\underline{\bar{\sigma}}}, \bar{\xi})$$
$$\text{with} \quad \bar{F}(\underline{\underline{\bar{\sigma}}}, \bar{\xi}) = \bar{q} - 3\alpha(\bar{\xi})\bar{p} - R(\bar{\xi}), \quad \bar{G}(\underline{\underline{\bar{\sigma}}}, \bar{\xi}) = \bar{q} - 3\beta(\bar{\xi})\bar{p} \tag{11}$$

where $\bar{p} = -\text{tr}(\underline{\underline{\bar{\sigma}}})/3$ is the mean stress value, $\bar{q} = \sqrt{3/2}\|\underline{\underline{\bar{\sigma}}}'\|$ is the stress deviator, $\underline{\underline{\bar{\sigma}}}'$ is the deviatoric part of the stress tensor, A, m, and F_0 are constant parameters, and α, R, and β are model parameters that may be expressed as functions of the viscoplastic hardening/softening variable $\bar{\xi}$, which is defined such that $\dot{\bar{\xi}} = \sqrt{2/3}\|\dot{\underline{\underline{\bar{\varepsilon}}}}'_{\text{vp}}\|$. In this study, all of the six viscoplastic model parameters were considered constant.

It is important to note that as the yield $\bar{F}$ and potential $\bar{G}$ functions of the fictitious isotropic material are expressed in terms of the fictitious stress $\underline{\underline{\bar{\sigma}}}$, that is $\underset{\sim}{L} : \underline{\underline{\hat{\sigma}}}$, the real yield F and potential G functions depend on both the stress tensor $\underline{\underline{\hat{\sigma}}}$ and the bedding orientation $\vec{e}$ such that

$$F(\underline{\underline{\hat{\sigma}}}, \vec{e}) = \bar{F}(\underline{\underline{\bar{\sigma}}}) = \bar{F}(\underset{\sim}{L}(\vec{e}) : \underline{\underline{\hat{\sigma}}}) \quad \text{and} \quad G(\underline{\underline{\hat{\sigma}}}, \vec{e}) = \bar{G}(\underline{\underline{\bar{\sigma}}}) = \bar{G}(\underset{\sim}{L}(\vec{e}) : \underline{\underline{\hat{\sigma}}}) \tag{12}$$

which means that the use of the $\underset{\sim}{L}$-transformation allows us to account for the non-elastic anisotropies (yield function and viscoplastic flow). The first equality means that $\underline{\underline{\hat{\sigma}}}$ reaches the real yield function $F(\underline{\underline{\hat{\sigma}}}, \vec{e}) = 0$ when $\underline{\underline{\bar{\sigma}}}$ reaches the fictitious yield $\bar{F}(\underline{\underline{\bar{\sigma}}}) = 0$. The second equality can be interpreted in the same way.

2.3. Hydraulic behavior

The liquid filtration velocity $\vec{w}^{\lambda}$, defined in equation (1), was assumed to respect the Darcy's law given as follows:

$$\vec{w}^{\lambda} = -\frac{\underline{\underline{K}}}{\eta_{\lambda}} \left(\vec{\nabla} p - \rho_{\lambda} \vec{g} \right) \tag{13}$$

where η_{λ} is the dynamic viscosity of the liquid phase and $\underline{\underline{K}}$ is the intrinsic permeability tensor. In general, the viscoplastic strain tensor $\underline{\underline{\varepsilon}}_{\mathrm{vp}}$ may induce a new hydraulic anisotropy in addition to the initial one (see, for example, Rutqvist, 2015). However, in this work, only an isotropic hydraulic alteration is considered. The permeability is thus obtained by multiplying the initial permeability tensor $\underline{\underline{K}}_0$ by a scalar factor, which varies with the tensor $\underline{\underline{\varepsilon}}_{\mathrm{vp}}$. The following expression was employed:

$$\underline{\underline{K}}(\varepsilon_{\mathrm{vp}}) = \left(1 + \kappa_c \left\langle \varepsilon_{\mathrm{vp}} \right\rangle^{\gamma_c} \right) \underline{\underline{K}}_0 \tag{14}$$

where only the positive part of $\varepsilon_{\mathrm{vp}} = \mathrm{tr}(\underline{\underline{\varepsilon}}_{\mathrm{vp}})$ is considered, and $\kappa_c \geq 0$ and $\gamma_c > 0$ are material constants. This expression, which is inspired by the multitude of permeability models in the literature (see, for example, Bary et al. (2000), Gawin et al. (2003), Picandet et al. (2001), and Saito (1995)), expresses the impact of an increase of the available space change on the fluids flow: it increases with dilatancy ($\varepsilon_{\mathrm{vp}} > 0$) and remains constant when the material is contractant ($\varepsilon_{\mathrm{vp}} < 0$). Indeed, as discussed in the experimental study of Zhang (2016), who examined the evolution of permeability in triaxial tests, and the homogenization study of Zhuang et al. (2017), the most important increase in permeability occurs when the volumetric strain

increases.

Regarding the mass density ρ_λ, the liquid phase was assumed to be moderately compressible, and its state law under isothermal conditions is given by

$$\frac{\dot{\rho}_\lambda}{\rho_\lambda} = \chi_\lambda \dot{p} \tag{15}$$

where χ_λ is the isothermal compressibility of the liquid phase.

2.4. Porosity evolution

Besides the stress partitioning (2) and permeability evolution law (14), the coupling between the mechanical and hydraulic problems needs also the evolution of the global porosity (Coussy, 1991), which is generally written as:

$$\dot{n} = (b - n)\dot{\varepsilon} + \dot{p}/M \tag{16}$$

where M is a constant material parameter (Biot modulus) and $\varepsilon = \mathrm{tr}(\underline{\underline{\varepsilon}})$ is the volumetric strain.

3. Case study: tunnel excavations in an argillaceous rock

The case study treats the excavation of two tunnels in the Callovo-Oxfordian (COx) claystone, an argillaceous rock that is under investigation by the French national radioactive waste management agency within the context of nuclear waste underground storage (ANDRA, 2012). The first tunnel, named GCS, has a circular section with a radius of 2.6 m and is excavated along the direction of the initial horizontal major stress. As for the second

tunnel, named GED, it has a horseshoe section with an average radius of 2.3 m and is excavated along the direction of the initial horizontal minor stress (see Fig. 2). At the level of those tunnels (490 m), the initial *in situ* stress state was estimated by Wileveau et al. (2007) such that the minor horizontal stress σ_h is nearly equal to the vertical stress σ_v ($\sigma_h \simeq \sigma_v \simeq 12\,\mathrm{MPa}$) and the horizontal major stress σ_H is approximately 30% larger than the two other components ($\sigma_H \simeq 16\,\mathrm{MPa}$).

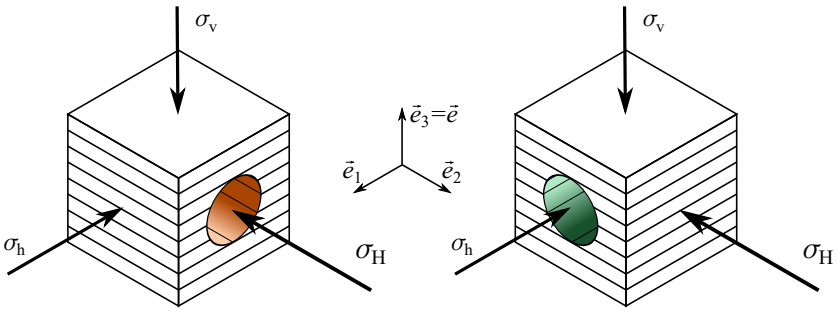


Figure 2: Schematic representation of the simulated tunnels with material anisotropy and initial stress state.

The field observations around those tunnels showed significant dissymmetry for the convergence and permeability measurements along with the shapes of the damaged zones (EDZ) (Armand et al., 2013, 2014; Guayacán-Carrillo et al., 2016). For the tunnel $//\sigma_h$, the EDZ are extended vertically, and the vertical convergence is approximately four times larger than the horizontal convergence. Regarding the tunnel $//\sigma_H$, the EDZ are extended horizontally, and the horizontal convergence is approximately two times larger than the vertical convergence.

An important research effort was made recently to model those excavations (Seyedi et al., 2017). For example, Martín et al. (2011) used a vis-

coplastic model that accounts for the anisotropies of the elastic parameters and creep behavior to reproduce the convergence measurements for the tunnel along the minor stress, but that model cannot reproduce the convergence measurements in the other direction ($//\sigma_{\mathrm{H}}$). Cuvilliez et al. (2017), Plassart et al. (2013), and Souley et al. (2017) used isotropic hydromechanical elasto-visco-plastic models for their simulations and focused only on the tunnel $//\sigma_{\mathrm{H}}$, whose cross section is subjected to an isotropic stress state $(\sigma_{\mathrm{h}}, \sigma_{\mathrm{v}})$. However, those works did not reproduce the convergence dissymmetry. Bian et al. (2017) also used an isotropic hydromechanical elasto-visco-plastic model. Although the model successfully reproduced different laboratory experiments, the results of the numerical simulations of the tunnels were not compared to the field measurements. Other works such as Mánica et al. (2017) and Pardoen and Collin (2017) used elasto-visco-plastic models for transversely isotropic materials. However, in these studies, the numerical results were presented only for the direction $//\sigma_{\mathrm{H}}$, which means that the calibrated parameters may not give a good representation for the convergence measurements in the other direction ($//\sigma_{\mathrm{h}}$).

In the current study, the convergence measurements for the two tunnels were considered simultaneously to ensure that the parameters have a better representation of the rock formation behavior. The use of the fictitious isotropic material approach helped us to reduce considerably the number of parameters and consequently simplified their identification.

3.1. Modeling setup

The numerical simulations were conducted using a 2D plane strain configuration where, for simplicity, the cross section was supposed circular in the

two tunnel directions, with radii of 2.6 m for GCS and 2.3 m for GED. The normal stress was set to $\underline{\underline{\sigma}}.\vec{n} = \Lambda \underline{\underline{\sigma_0}}.\vec{n}$, where $\underline{\underline{\sigma_0}} = -\mathrm{diag}(\sigma_\mathrm{h}, \sigma_\mathrm{H}, \sigma_\mathrm{v})$ is the initial stress tensor, $\vec{n}$ is the normal to the tunnel wall, and Λ is a deconfining function that decreases in a non-linear manner from 1 to 0 over a period of 30 days and remains zero after the excavation period (see Fig. 3). Similar to the *in situ* conditions, the convergence measurements starts at a time t_0 fixed to 15 days, corresponding to the excavation front passage. Concerning the hydraulic part, the material was supposed to remain water-saturated during all the simulation time and the liquid pressure at the tunnel wall was reduced from the *in situ* pressure (4.7 MPa) to atmospheric pressure (0.1 MPa), as represented in Fig. 3. All the numerical simulations were carried out using the finite element software Code-Aster (`www.code-aster.com`).

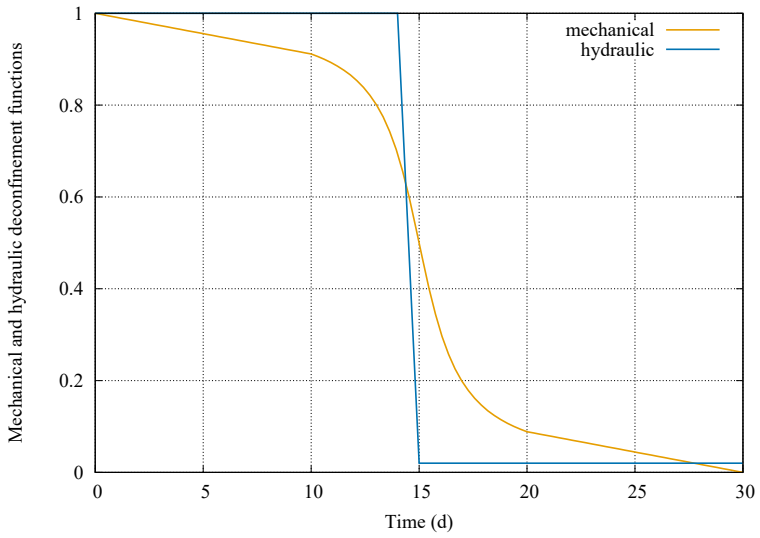
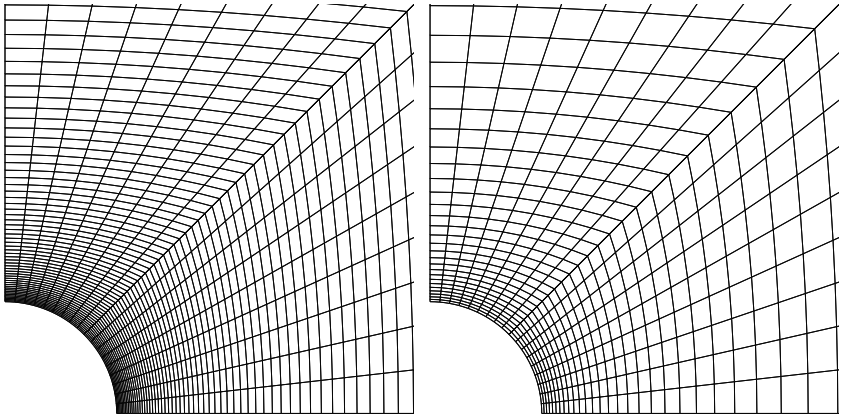


Figure 3: Mechanical and hydraulic deconfining functions employed to simulate tunnels excavations and based on field measurements.

The model parameters are presented in Table 1. They were based on the

available laboratory measurements for the COx claystone, except for the viscoplastic and permeability evolution parameters, which were fitted to the *in situ* measurements. The experimental studies on the COx claystone showed that the permeability anisotropy is less marked than the mechanical behavior anisotropy (ANDRA, 2012). For that reason, the initial permeability tensor was assumed isotropic in our simulations ($\underline{\underline{K}}_0 = K_0\underline{\underline{1}}$).

A second-order quadrangular structured mesh (see Fig. 4(a)) was employed for all of the simulations. The mesh distribution was chosen to be nearly symmetric next to the tunnel's wall to avoid localization problems owing to mesh disymmetry. The size of the elements varies from $R/100$ next to the drift wall to $0.4R$ far from it (at $10R$). To make sure that the obtained results are not mesh dependent, a second coarser mesh (see Fig. 4(a)) was tested. Fig. 5 represents a comparison between the obtained results with the two meshes. It is clear from the figure that the two results are almost identical.



(a) Fine mesh (b) Coarse mesh

Figure 4: Illustration of the fine and coarse meshes in the vicinity of the tunnel.

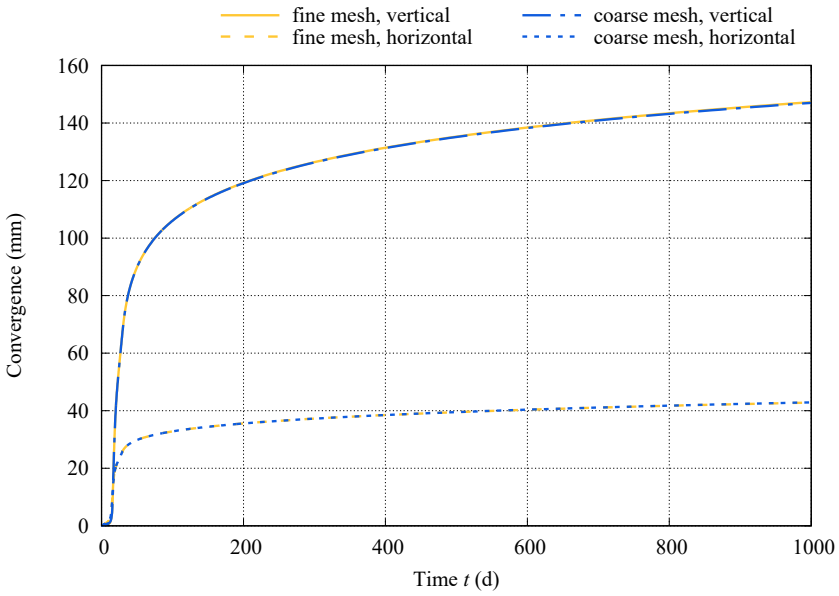


Figure 5: Vertical and horizontal convergences of the tunnel $//\sigma_{\mathrm{h}}$ using two different meshes and the parameters M-I from Table 1.

To effectively identify the various model parameters, a three-step procedure, where the problem complexity was progressively increased, was employed: (1) a pure mechanical problem with an isotropic material (M-I), (2) a pure mechanical problem with a transversely isotropic material (M-TI), and (3) a fully coupled hydromechanical problem with a transversely isotropic material (HM-TI).

3.2. Modeling results and comparison with field data

For the first simulation assumptions (M-I), the only involved anisotropy is due to the initial stress state ($\sigma_{\mathrm{H}} > \sigma_{\mathrm{h}} = \sigma_{\mathrm{v}}$). Hence, theoretically, the dissymmetry in the tunnel $//\sigma_{\mathrm{H}}$, whose cross section is subjected to an isotropic stress $(\sigma_{\mathrm{h}}, \sigma_{\mathrm{v}})$, could not be reproduced. Fig. 6 shows the obtained numerical results for the convergence measurements in comparison with the field data.

Table 1: Hydromechanical model parameters used to simulate the excavation of the two tunnels (M: Mechanical, HM: Hydromechanical, I: Isotropic, TI: Transverse Isotropic).

Equation / name	**Parameter**	**Value**		
		M-I	M-TI	HM-TI
Real anisotropic material	E(MPa)	-	6 000	6 000
	E'(MPa)	-	4 500	4 000
	ν	-	0.2	0.2
	ν	-	0.2	0.2
	G	-	2 187.5	2 083.33
Fictitious isotropic material	$\bar{E}$(MPa)	5600	4500	4000
	$\bar{\nu}$	0.2	0.2	0.2
Viscoplastic law	$A(\mathrm{d}^{-1})$	2×10^{-13}	2×10^{-13}	2×10^{-13}
	m	6	6	6
	F_0(MPa)	0.1	0.1	0.1
	α	0	0	0
	R(MPa)	9	9.8	8.5
	β	0.3	0.38	0.39
Porosity evolution	$n(t=0)$	-	-	0.14
	b	-	-	0.6
	M(GPa)	-	-	16.9
Permeability law	$K_0(\mathrm{m}^2)$	-	-	2×10^{-20}
	κ_c	-	-	10^{11}
	γ_c	-	-	3
Dynamic viscosity	$\eta_\lambda(\mathrm{Pa \cdot s})$	-	-	10^{-3}
Isothermal compressibility	$\chi_\lambda(\mathrm{MPa}^{-1})$	-	-	5×10^{-4}

The model explains well the measurements in the direction of the minor stress ($//\sigma_\mathrm{h}$) for both the horizontal and vertical convergences. As for the direction of the major stress ($//\sigma_\mathrm{H}$), an overall agreement with the experimental data was obtained. However, as expected, the isotropic material assumption could not explain the differences between the horizontal and vertical convergences.

For the second simulation type (M-TI), as the material anisotropy was considered, better results were obtained in the direction $//\sigma_\mathrm{H}$ (see Fig. 7).

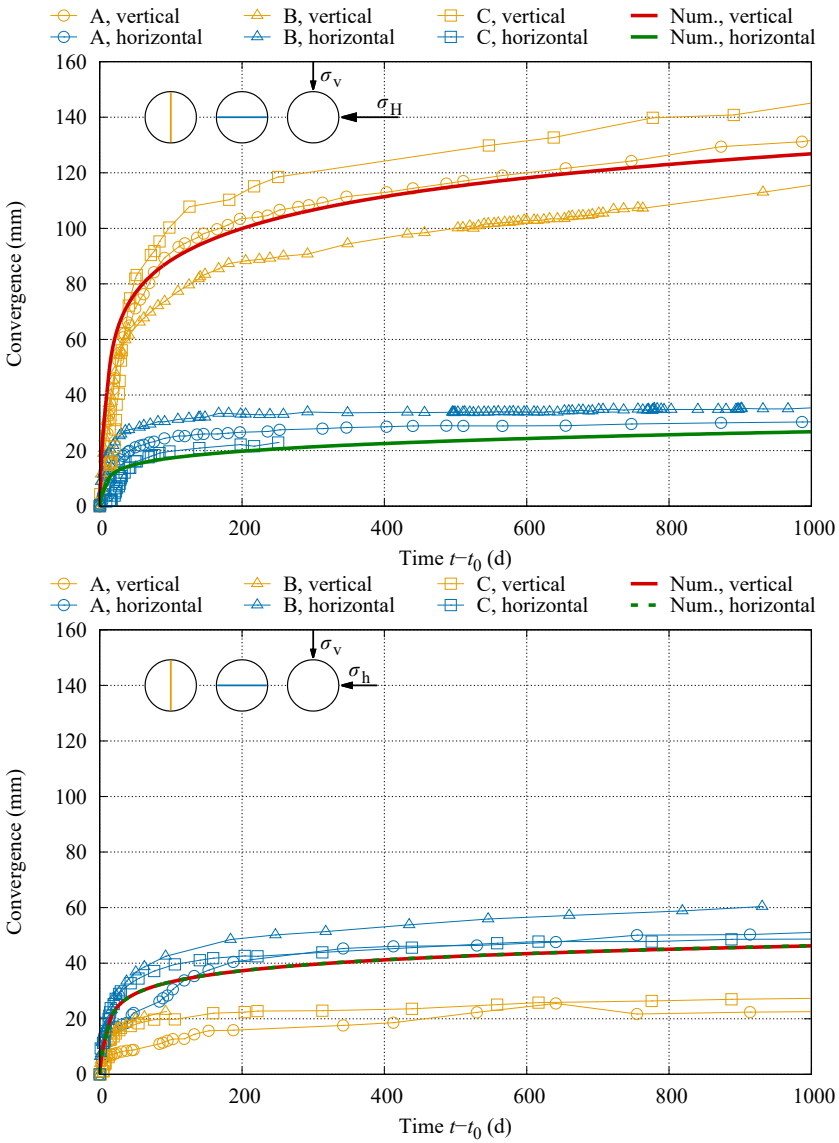


Figure 6: Vertical and horizontal convergence measurements with the M-I simulations for the two tunnels parallel to σ_h (top) and σ_H (bottom) compared to data from three sections, A, B, and C, of each tunnel.

The viscoplastic parameters were slightly modified compared to the previous simulations to get a simultaneous good fitting with the horizontal and

vertical convergence measurements in the two tunnel directions. In fact, a combination between the material and initial stress state anisotropies led to the dissymmetry in the tunnel $//\sigma_{\mathrm{h}}$, whereas in the isotropic case (M-I) that dissymmetry was explained only by the initial stress state anisotropy.

To better understand the origin of the dissymmetry in the convergence results, the deviatoric stress was recorded at the tunnel ceiling and side wall for the two previous simulations. These results are presented in Fig. 8 along with the results of the elastic computations, used as a reference. For the tunnel $//\sigma_{\mathrm{h}}$, it is clear that the elastic yield is crossed (the curve is detached from the elastic results) at the ceiling before the side wall, which allows viscoplasticity and the resulting dilatancy to develop more at the ceiling. Consequently, the vertical convergence is higher than the horizontal convergence. Regarding the tunnel $//\sigma_{\mathrm{H}}$, the elastic yield is crossed at the side wall before the ceiling. This observation is only true for the M-TI simulation, because, in the M-I case, the ceiling and side wall have the same behavior. The difference is less clear than that in the other tunnel because the dissymmetry is less marked. One may follow the dashed lines representing the elastic results to visualize this difference.

The obtained parameters from the previous simulations could be regarded as the undrained parameters. In fact, as the material permeability is very low (approximately 10^{-20} m^2), it may be reasonable to assume that the flow of the ground water is negligible, and thus, to use directly the undrained parameters. However, for the sake of completeness of our work, the hydromechanical coupling in a transversely isotropic material (HM-TI) was also considered. Fig. 9 shows the obtained numerical results compared to the experimental

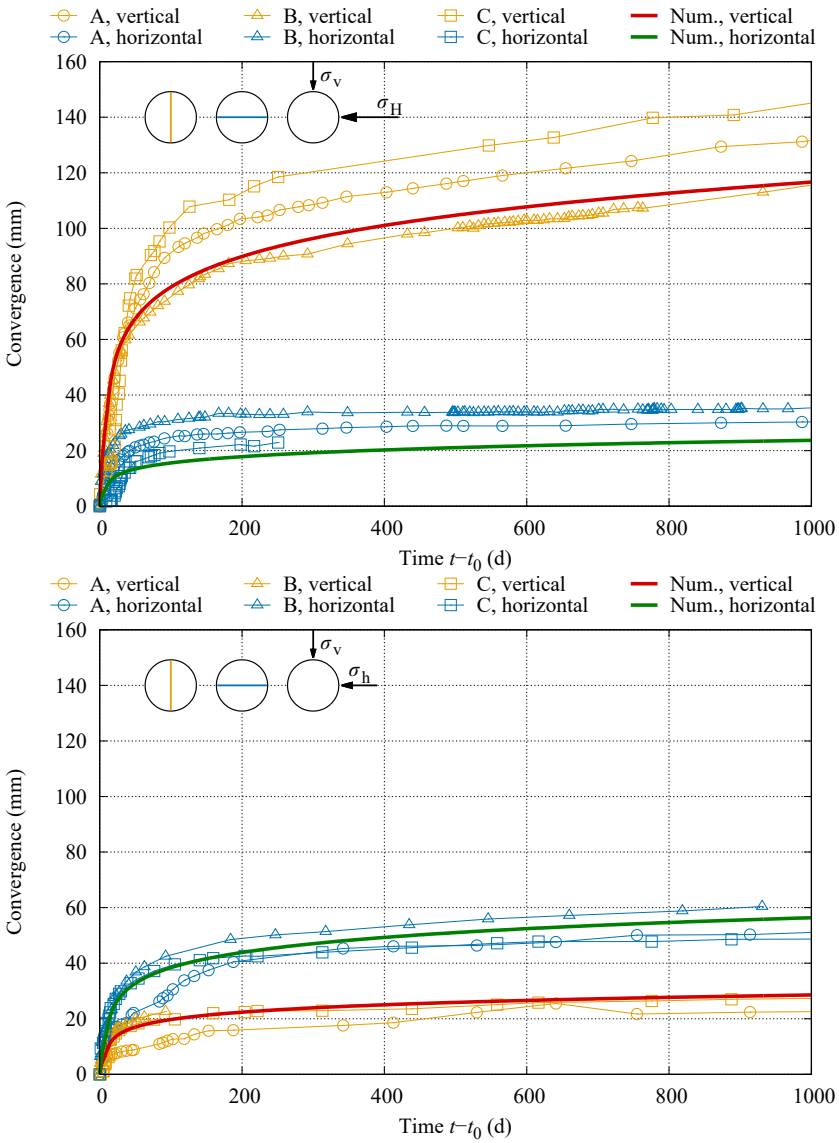
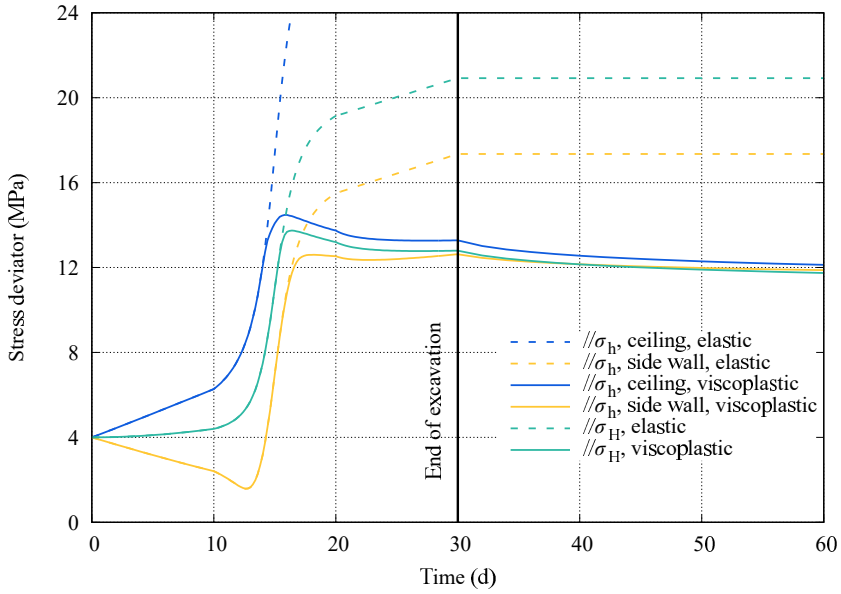
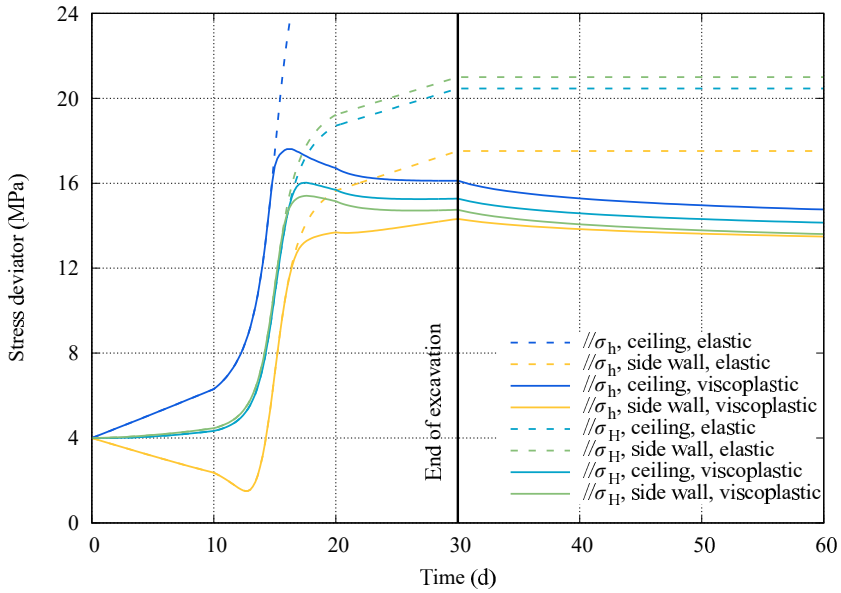


Figure 7: Vertical and horizontal convergence measurements with the M-TI simulations for the two tunnels parallel to σ_h (top) and σ_H (bottom) compared to data from three sections, A, B, and C, of each tunnel.

data. As can be seen, the predicted values of the convergence measurements are in good agreement with the experimental data for the two tunnel direc-



(a) M-I



(b) M-TI

Figure 8: Stress deviator at the ceiling and side wall of the two tunnels $//\sigma_{\mathrm{h}}$ and $//\sigma_{\mathrm{H}}$.

tions ($//\sigma_{\mathrm{h}}$ and $//\sigma_{\mathrm{H}}$) and for both the ceiling and the side wall. Compared to the M-TI model parameters, the obtained parameters were not very different. The main difference was for the model constant R, which was reduced owing to the effect of the pore pressure in the definition of the effective stress.

Regarding the hydraulic response, the parameters κ_c and γ_c were fitted to the field permeability measurements published by Armand et al. (2014). Fig. 10 shows these measurements, along the horizontal and vertical directions around the tunnel, compared to the model results. As can be observed, the obtained results are in an overall accordance with the measurements in spite of the discrepancy of the experimental points.

To study the time effect on the EDZ hydraulic properties, the permeability evolutions at the ceiling and side wall of the two tunnels are represented in Fig. 11. The permeability increases dramatically during the excavation process and stabilizes rapidly afterwards. This aspect is clarified further in Fig. 12, in which the evolution in both time and space are presented. It is clear that the disturbed areas around the tunnels have globally the same shape as the *in situ* observations (Armand et al., 2013, 2014): the EDZ is extended vertically in the direction $//\sigma_{\mathrm{h}}$ and horizontally in the direction $//\sigma_{\mathrm{H}}$.

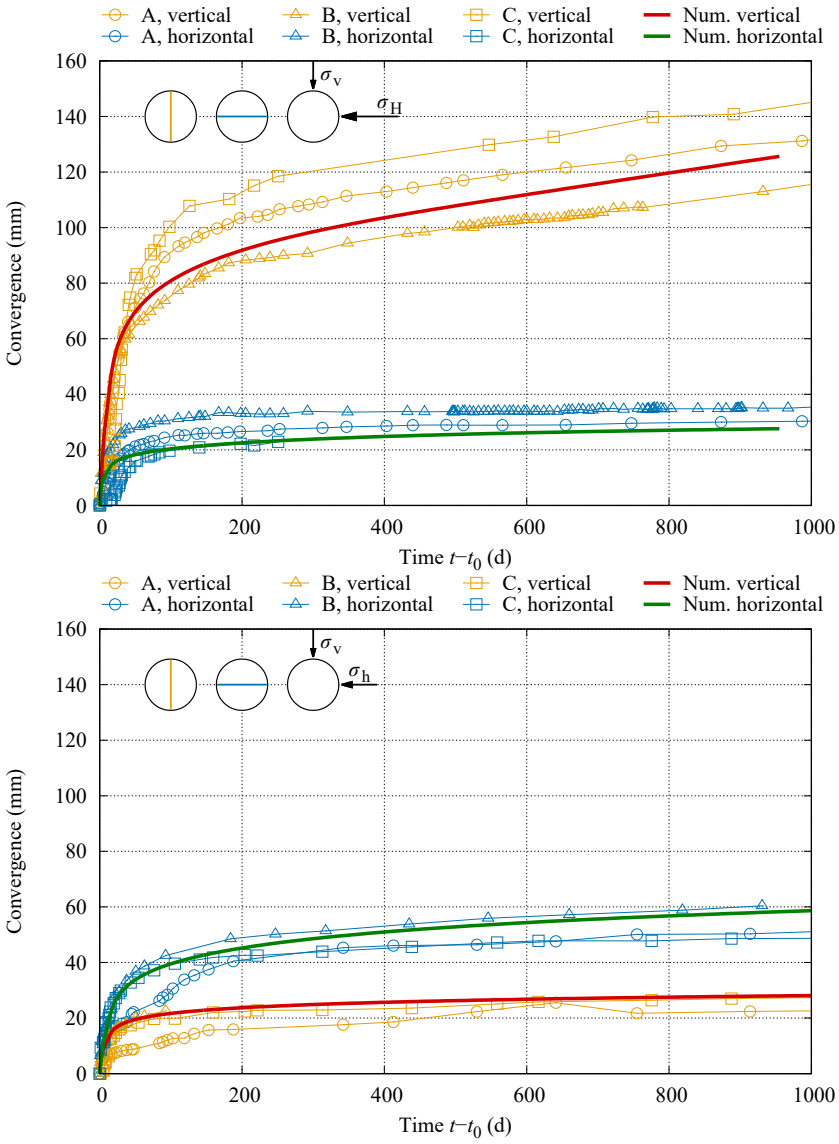


Figure 9: Vertical and horizontal convergence measurements with the HM-TI simulations for the two tunnels parallel to σ_h (top) and σ_H (bottom) compared to data from three sections, A, B, and C, of each tunnel.

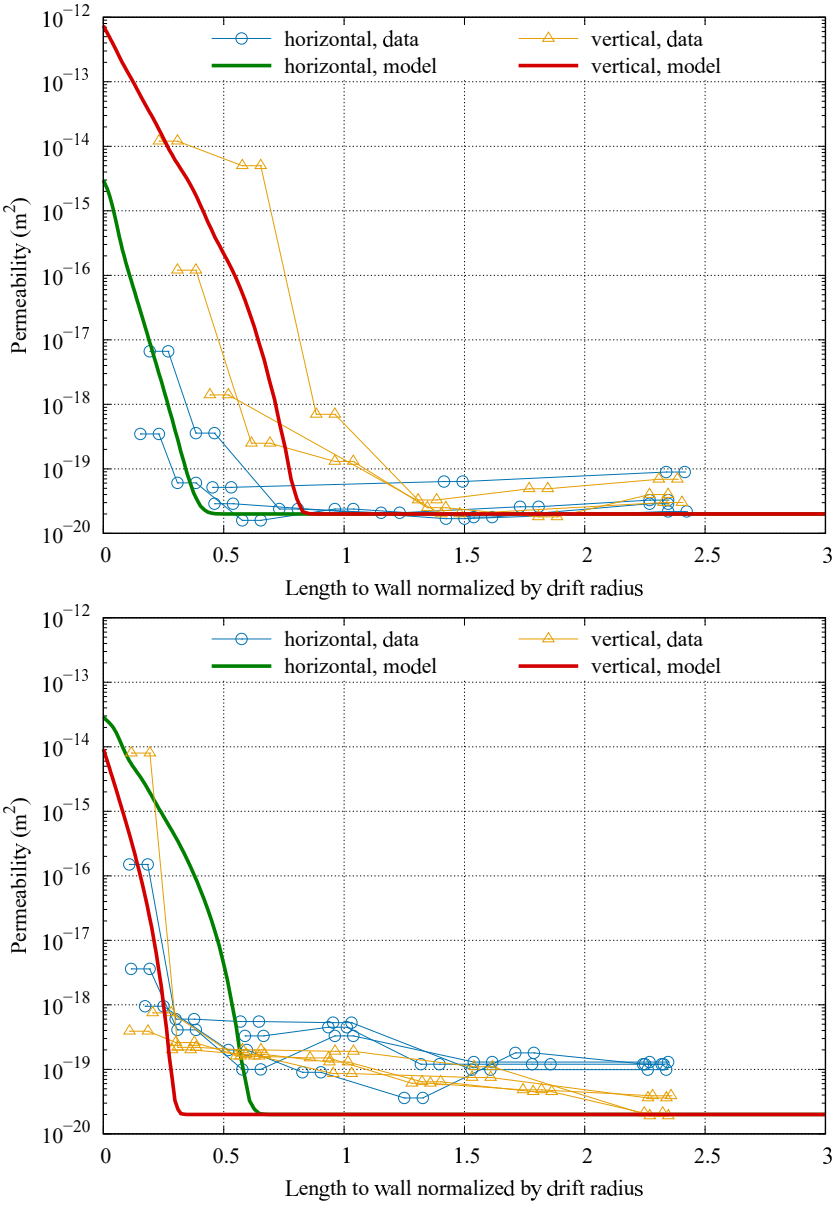


Figure 10: Variation of the permeability around the tunnels $//\sigma_h$ (top) and $//\sigma_H$ (bottom), 100 days after beginning excavation.

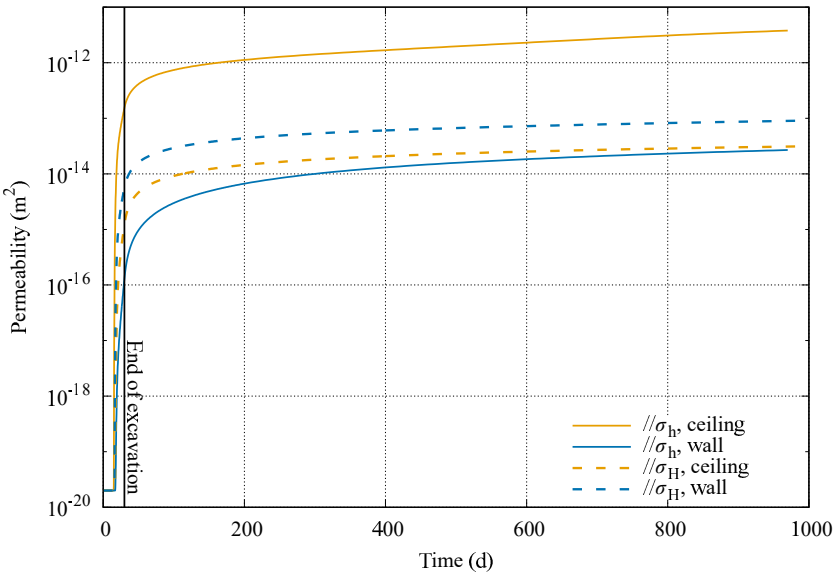


Figure 11: Permeability at the ceiling and side wall as function of time.

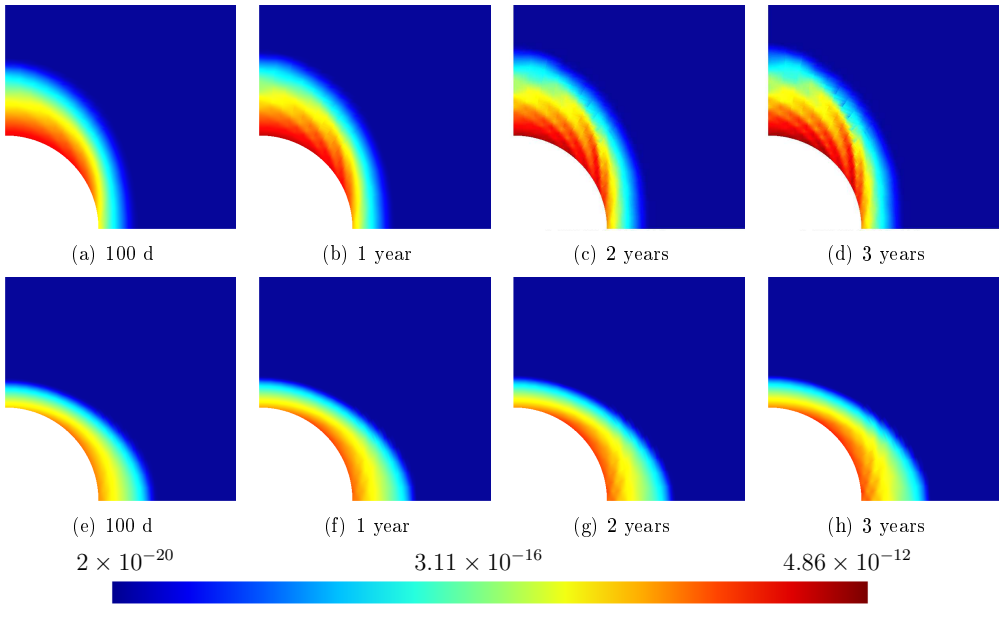


Figure 12: Permeability // σ_h (a to d) and // σ_H (e to h).

4. Conclusions and perspectives

In this paper, a new hydromechanical constitutive model, which accounts for elastic and non-elastic anisotropies, time-dependent behavior, and permeability alteration, was proposed. It was based on an equivalence approach between the real transversely isotropic material and a fictitious isotropic material. Although the mathematical formalism seems very complex, the obtained method was practical as it allows the use of classical constitutive models for isotropy to obtain new models for transverse isotropy, including both elastic and non-elastic material anisotropies.

The constitutive model was implemented in a numerical software (Code-Aster) and was applied to the analysis of the field measurements regarding two tunnels excavated in the direction of the minor and major horizontal stresses. The viscoplastic parameters were identified for three difficulty levels, namely, mechanical simulations with isotropic and transverse isotropic materials, and fully coupled hydromechanical simulations with a transversely isotropic material. The obtained numerical results were in a good agreement with *in situ* data, especially for the convergence measurements. The model was able to reproduce the vertical and horizontal measurements in both tunnel directions, using a single set of parameters.

Although the ability of the model to capture the main relevant phenomena associated to the material anistropy is rather satisfactory, further investigations are required to complete the proposed approach and increase the reliability of its predictive capacity. Two of the most important necessary studies focus on: (i) coupling with the instantaneous plasticity in order to better describe the short-term material response and (ii) accounting for

both the initial and induced anisotropies in the permeability tensor and Biot coefficient.

Acknowledgments

The authors are grateful to ANDRA for providing the *in situ* convergence and permeability measurements.

Appendix A. Analytical expression of the isotropy-transverse isotropy transformation

To simplify the analytical determination of the $\underset{\sim}{L}$-transformation components, a special basis of the symmetric second order tensors space $\mathcal{S}$ is employed. Given $B = (\vec{e}_1, \vec{e}_2, \vec{e}_3 = \vec{e})$ an orthonormal basis of $\mathbb{R}^3$, where $\vec{e}$ is a normal vector to the bedding plane, the canonical basis of $\mathcal{S}$ may be written as

$$\begin{gathered} \underline{\underline{e}}_1 = \vec{e}_1 \otimes \vec{e}_1, \quad \underline{\underline{e}}_2 = \vec{e}_2 \otimes \vec{e}_2, \quad \underline{\underline{e}}_3 = \vec{e}_3 \otimes \vec{e}_3, \\ \underline{\underline{e}}_4 = \frac{1}{\sqrt{2}}(\vec{e}_1 \otimes \vec{e}_2 + \vec{e}_2 \otimes \vec{e}_1), \quad \underline{\underline{e}}_5 = \frac{1}{\sqrt{2}}(\vec{e}_1 \otimes \vec{e}_3 + \vec{e}_3 \otimes \vec{e}_1), \\ \underline{\underline{e}}_6 = \frac{1}{\sqrt{2}}(\vec{e}_2 \otimes \vec{e}_3 + \vec{e}_3 \otimes \vec{e}_2) \end{gathered} \tag{A.1}$$

The special basis of $\mathcal{S}$ is defined by

$$\begin{gathered} \underline{\underline{I}} = \underline{\underline{1}}/\sqrt{3}, \ \underline{\underline{J}}_1 = (\underline{\underline{1}} - 3\underline{\underline{e}}_3)/\sqrt{6}, \ \underline{\underline{J}}_2 = (\underline{\underline{e}}_1 - \underline{\underline{e}}_2)/\sqrt{2}, \\ \underline{\underline{J}}_3 = \underline{\underline{e}}_4, \quad \underline{\underline{J}}_4 = \underline{\underline{e}}_5, \quad \underline{\underline{J}}_5 = \underline{\underline{e}}_6 \end{gathered} \tag{A.2}$$

In this basis, a transversely isotropic tensor $\underset{\sim}{A}$ can be expressed as

$$\begin{aligned}\underset{\sim}{A} = a_1 \underset{=}{I}\otimes\underset{=}{I} + a_2\left(\underset{=}{I}\otimes\underset{=}{J}_1 + \underset{=}{J}_1\otimes\underset{=}{I}\right) + a_3\underset{=}{J}_1\otimes\underset{=}{J}_1 \\ +a_4\left(\underset{=}{J}_2\otimes\underset{=}{J}_2 + \underset{=}{J}_3\otimes\underset{=}{J}_3\right) + a_5\left(\underset{=}{J}_4\otimes\underset{=}{J}_4 + \underset{=}{J}_5\otimes\underset{=}{J}_5\right)\end{aligned} \tag{A.3}$$

which has the advantage of showing four eigenvectors of $\underset{\sim}{A}$: $(\underset{=}{J}_2, \underset{=}{J}_3, \underset{=}{J}_4, \underset{=}{J}_5)$ to which are associated the eigenvalues (a_4, a_4, a_5, a_5). Consequently, $\underset{\sim}{A}$ could be completely defined by two eigenvalues (a_4, a_5) and a 2×2 matrix $[\boldsymbol{A}] = \begin{pmatrix} a_1 & a_2 \\ a_2 & a_3 \end{pmatrix}$ in the basis $(\underset{=}{I}, \underset{=}{J}_1)$.

Let ℓ_i, h_i, and $\bar{h}_i$ $(i = 1 \dots 5)$ be, respectively, the components of $\underset{\sim}{L}$, $\underset{\sim}{H}^{-1}$, and $\underset{\sim}{\bar{H}}^{-1}$ in this basis. It follows from equation (7)

$$\begin{aligned}[\boldsymbol{L}] = [\bar{\boldsymbol{H}}^{\frac{1}{2}}]\left([\bar{\boldsymbol{H}}^{-\frac{1}{2}}][\boldsymbol{H}^{-1}][\bar{\boldsymbol{H}}^{-\frac{1}{2}}]\right)^{\frac{1}{2}}[\bar{\boldsymbol{H}}^{\frac{1}{2}}], \\ \ell_4 = \sqrt{h_4/\bar{h}_4}, \quad \ell_5 = \sqrt{h_5/\bar{h}_5}\end{aligned} \tag{A.4}$$

Finally, the resolution of the first relation in this equation leads to the following expressions of ℓ_i as function of (E, E', ν, ν', G) and $(\bar{E}, \bar{\nu})$:

$$\begin{aligned}\ell_1 = \sqrt{\bar{E}}\Big(h_1 + \sqrt{(\bar{b}/\bar{a})}\gamma\Big)/\Delta, \quad \ell_2 = \sqrt{\bar{E}}\, h_2/\Delta, \\ \ell_3 = \sqrt{\bar{E}}\Big(h_3 + \sqrt{(\bar{a}/\bar{b})}\gamma\Big)/\Delta, \quad \ell_4 = \sqrt{\bar{E}}\sqrt{h_4/\bar{b}}, \\ \ell_5 = \sqrt{\bar{E}}\sqrt{h_5/\bar{b}}\end{aligned} \tag{A.5}$$

where $\bar{a} = 1-2\bar{\nu}$, $\quad \bar{b} = 1+\bar{\nu}$, $\quad \gamma = \sqrt{h_1 h_3 - h_2^2}$, $\Delta = \sqrt{\bar{a}h_1 + \bar{b}h_3 + 2\sqrt{\bar{a}\bar{b}}\gamma}$,

and h_i and $\bar{h}_i$ are expressed as follows:

$$
\begin{aligned}
h_1 &= \frac{1}{3}\left[2(1-\nu)/E + (1-4\nu')/E'\right], \\
h_2 &= \frac{\sqrt{2}}{3}\left[(1-\nu)/E - (1-\nu')/E'\right], \\
h_3 &= \frac{1}{3}\left[(1-\nu)/E + 2(1+2\nu')/E'\right], \\
h_4 &= (1+\nu)/E, \quad h_5 = 1/2G, \\
\bar{h}_1 &= (1-2\bar{\nu})/\bar{E}, \quad \bar{h}_2 = 0, \\
\bar{h}_3 &= \bar{h}_4 = \bar{h}_5 = (1+\bar{\nu})/\bar{E}
\end{aligned}
\tag{A.6}
$$

References

ANDRA, 2012. Référentiel du comportement THM des formations sur le site de Meuse / Haute-Marne. Tech. Rep. D.RP.AMFS.1 2.0024, ANRDA.

Armand, G., Leveau, F., Nussbaum, C., de La Vaissiere, R., Noiret, A., Jaeggi, D., Landrein, P., Righini, C., 2014. Geometry and properties of the excavation-induced fractures at the meuse/haute-marne url drifts. Rock Mechanics and Rock Engineering 47 (1), 21–41.

Armand, G., Noiret, A., Zghondi, J., Seyedi, D., 2013. Short- and long-term behaviors of drifts in the Callovo-Oxfordian claystone at the Meuse/Haute-Marne underground research laboratory. Journal of Rock Mechanics and Geotechnical Engineering 5, 221–230.

Barla, G., 2001. Tunnelling under squeezing rock conditions. Eurosummer-School in Tunnel Mechanics, Innsbruck, 169–268.

Barla, G., Bonini, M., Debernardi, D., 2010. Time dependent deformations in

squeezing tunnels. ISSMGE International Journal of Geoengineering Case Histories 2 (1), 40–65.

Bary, B., Bournazel, J.-P., Bourdarot, E., 2000. Poro-damage approach applied to hydro-fracture analysis of concrete. Journal of Engineering Mechanics 126 (9), 937–943.

Bertrand, F., Collin, F., 2017. Anisotropic modelling of opalinus clay behaviour: From triaxial tests to gallery excavation application. Journal of Rock Mechanics and Geotechnical Engineering.

Bian, H., Zhang, X., Shao, J., 2017. A coupled elastoplastic and visco-plastic damage model for hard clay and its application for the underground gallery excavation. Underground Space 2 (1), 60 – 72.

Biot, M. A., 1941. General theory of three-dimensional consolidation. Journal of Applied Physics 12 (2), 155 – 164.

Bonini, M., Debernardi, D., Barla, M., Barla, G., 2009. The mechanical behaviour of clay shales and implications on the design of tunnels. Rock mechanics and rock engineering 42 (2), 361–388.

Coussy, O., 1991. Mécanique des milieux poreux. Editions Technip.

Cuvilliez, S., Djouadi, I., Raude, S., Fernandes, R., 2017. An elastoviscoplastic constitutive model for geomaterials: Application to hydromechanical modelling of claystone response to drift excavation. Computers and Geotechnics 85, 321–340.

Gawin, D., Pesavento, F., Schrefler, B., 2003. Modelling of hygro-thermal behaviour of concrete at high temperature with thermo-chemical and mechanical material degradation. Computer methods in applied mechanics and engineering 192 (13), 1731–1771.

Gesta, P., 1994. Travaux souterrains (ref. article : c5565), fre.
URL https://www.techniques-ingenieur.fr

Guayacán-Carrillo, L.-M., Sulem, J., Seyedi, D. M., Ghabezloo, S., Noiret, A., Armand, G., 2016. Analysis of long-term anisotropic convergence in drifts excavated in callovo-oxfordian claystone. Rock Mechanics and Rock Engineering 49 (1), 97–114.

Kim, C., Baek, S., Hong, S., 2005. Tunnel convergence analyses in heterogeneous/anisotropic rock masses. In: International world tunnel congress and the 31st ITA General Assembly, Istanbul, Turkey. pp. 1091–1097.

Klopčič, J., Logar, J., 2014. Effect of relative orientation of anisotropy planes to tunnel axis on the magnitude of tunnelling displacements. International Journal of Rock Mechanics and Mining Sciences 71, 235–248.

Mahjoub, M., Rouabhi, A., Tijani, M., Granet, S., 2015. An approach to model the mechanical behavior of transversely isotropic materials. International Journal for Numerical and Analytical Methods in Geomechanics 40, 942–961.

Manh, H. T., Sulem, J., Subrin, D., Billaux, D., 2015. Anisotropic time-dependent modeling of tunnel excavation in squeezing ground. Rock Mechanics and Rock Engineering 48 (6), 2301–2317.

Manh, H. T., Sulem, J., Subrin, D., et al., 2014. Analysis of the geotechnical data monitored during Saint-Martin-la-Porte access gallery excavation. In: ISRM Regional Symposium-EUROCK 2014. International Society for Rock Mechanics.

Mánica, M., Gens, A., Vaunat, J., Ruiz, D., 2016. A cross-anisotropic formulation for elasto-plastic models. Géotechnique Letters 6 (2), 156–162.

Mánica, M., Gens, A., Vaunat, J., Ruiz, D. F., 2017. A time-dependent anisotropic model for argillaceous rocks. application to an underground excavation in callovo-oxfordian claystone. Computers and Geotechnics 85, 341–350.

Martín, L. B., Hadj-Hassen, F., Tijani, M., Armand, G., 2011. New numerical modelling of the mechanical long-term behaviour of the GMR gallery in ANDRA's Underground Research Laboratory. Physics and Chemistry of the Earth, Parts A/B/C 36 (17), 1872–1877.

Panet, M., 1995. Le calcul des tunnels par la méthode convergence - confinement. Presses de l'ENPC.

Panet, M., 1996. Two case histories of tunnels through squeezing rocks. Rock mechanics and rock engineering 29 (3), 155–164.

Pardoen, B., Collin, F., 2017. Modelling the influence of strain localisation and viscosity on the behaviour of underground drifts drilled in claystone. Computers and Geotechnics 85, 351–367.

Pardoen, B., Talandier, J., Collin, F., 2016. Permeability evolution and water

transfer in the excavation damaged zone of a ventilated gallery. International Journal of Rock Mechanics and Mining Sciences 85, 192–208.

Pellet, F., 2009. Contact between a tunnel lining and a damage-susceptible viscoplastic medium. Comput Model Eng Sci 52 (3), 279–295.

Picandet, V., Khelidj, A., Bastian, G., 2001. Effect of axial compressive damage on gas permeability of ordinary and high-performance concrete. Cement and Concrete Research 31, 1525–1532.

Plana, D., López, C., Cornelles, J., Muñoz, P., 2004. Numerical analysis of a tunnel in an anisotropy rock mass. Envalira tunnel (principality of Andorra). In: Engineering Geology for Infrastructure Planning in Europe. Springer, pp. 153–161.

Plassart, R., Fernandes, R., Giraud, A., Hoxha, D., Laigle, F., 2013. Hydromechanical modelling of an excavation in an underground research laboratory with an elastoviscoplastic behaviour law and regularization by second gradient of dilation. International Journal of Rock Mechanics and Mining Sciences 58, 23–33.

Prassetyo, S. H., Gutierrez, M., 2016. Effect of surface loading on the hydromechanical response of a tunnel in saturated ground. Underground Space 1 (1), 1 – 19.

Rahal, S., Sellier, A., Casaux-Ginestet, G., 2017. Poromechanical consolidation and basic creep interactions around tunnel excavation. International Journal of Rock Mechanics and Mining Sciences 94, 55–63.

Rutqvist, J., 2015. Fractured rock stress-permeability relationships from in situ data and effects of temperature and chemical-mechanical couplings. Geofluids 15 (1-2), 48–66.

Saito, M., 1995. Chloide permeability of concrete under static and repeated compressive loading. Cement and Concrete Research 25 (4), 803–808.

Seyedi, D. M., Armand, G., Noiret, A., 2017. "Transverse Action"–A model benchmark exercise for numerical analysis of the Callovo-Oxfordian claystone hydromechanical response to excavation operations. Computers and Geotechnics 85, 287–305.

Soga, K., Laver, R. G., Li, Z., 2017. Long-term tunnel behaviour and ground movements after tunnelling in clayey soils. Underground Space 2 (3), 149 – 167.

Souley, M., Armand, G., Kazmierczak, J.-B., 2017. Hydro-elasto-viscoplastic modeling of a drift at the meuse/haute-marne underground research laboratoratory (url). Computers and Geotechnics 85, 306–320.

Tao, F., Bobet, A., 2016. Effect of temperature on deep lined circular tunnels in transversely anisotropic elastic rock. Underground Space 1 (2), 79 – 93.

Tonon, F., Amadei, B., 2002. Effect of elastic anisotropy on tunnel wall displacements behind a tunnel face. Rock mechanics and rock engineering 35 (3), 141–160.

Tonon, F., Amadei, B., 2003. Stresses in anisotropic rock masses: an engineering perspective building on geological knowledge. International Journal of Rock Mechanics and Mining Sciences 40 (7), 1099–1120.

Vu, T. M., Sulem, J., Subrin, D., Monin, N., Mar 2013a. Semi-analytical solution for stresses and displacements in a tunnel excavated in transversely isotropic formation with non-linear behavior. Rock Mechanics and Rock Engineering 46 (2), 213–229.

Vu, T. M., Sulem, J., Subrin, D., Monin, N., Lascols, J., Mar 2013b. Anisotropic closure in squeezing rocks: The example of saint-martin-la-porte access gallery. Rock Mechanics and Rock Engineering 46 (2), 231–246.

Wang, T.-T., Huang, T.-H., 2011. Numerical simulation on anisotropic squeezing phenomenon of new guanyin tunnel. Journal of GeoEngineering 6 (3), 125–133.

Wileveau, Y., Cornet, F., Desroches, J., Blumling, P., 2007. Complete in situ stress determination in an argillite sedimentary formation. Physics and Chemistry of the Earth, Parts A/B/C 32 (8), 866–878.

Zhang, C.-L., 2016. The stress–strain–permeability behaviour of clay rock during damage and recompaction. Journal of Rock Mechanics and Geotechnical Engineering 8 (1), 16–26.

Zhuang, X., Huang, R., Liang, C., Rabczuk, T., 2014. A coupled thermo-hydro-mechanical model of jointed hard rock for compressed air energy storage. Mathematical Problems in Engineering 2014.

Zhuang, X., Wang, Q., Zhu, H., 2017. Multiscale modelling of hydro-mechanical couplings in quasi-brittle materials. International Journal of Fracture 204 (1), 1–27.